

See discussions, stats, and author profiles for this publication at: <https://www.researchgate.net/publication/255756149>

Twist disclination loops in a bent-core nematic liquid crystal

ARTICLE *in* SOFT MATTER · JUNE 2011

Impact Factor: 4.03 · DOI: 10.1039/C1SM05245D

CITATIONS

3

READS

12

3 AUTHORS, INCLUDING:



[K. S. - Krishnamurthy](#)

Centre for Nano and Soft Matter Sciences (f...

41 PUBLICATIONS 239 CITATIONS

SEE PROFILE



[Pramod Tadapatri](#)

Raman Research Institute

9 PUBLICATIONS 76 CITATIONS

SEE PROFILE

Cite this: *Soft Matter*, 2011, **7**, 6273

www.rsc.org/softmatter

PAPER

Twist disclination loops in a bent-core nematic liquid crystal†

Kanakapura S. Krishnamurthy,^{*a} Pramod Tadapatri^a and Wolfgang Weissflog^b

Received 14th February 2011, Accepted 15th April 2011

DOI: 10.1039/c1sm05245d

We report on the generation and stability of half-strength twist disclination loops separating planar and π -twisted regions in a bent-core nematic liquid crystal with planar anchoring. Loops L(P) and L(T) surrounding planar and π -twisted domains, respectively, are both generated during relaxation from the quasi-homeotropic splay-Freedericksz state. We demonstrate that the metastable twisted state occurs as a rule in the region of lateral separation of singular loops formed *via* wall pincement and collapsing at different rates. The results provide the first experimental confirmation of the early theoretical prediction that, for circular loops L(P), there exists a critical radius R_c separating regimes of growth and decay. R_c varies with temperature indicating its dependence on elastic anisotropy. R , which changes quasistatically around R_c , is linear in time in the long thread regime for both L(P) and L(T). An earlier model for L(T) is extended for L(P) to fully account for the observed dynamics of both subcritical and supercritical loops, and also to extract the related viscoelastic parameter.

1 Introduction

Topological defects in nematic liquid crystals have been a subject of profound scientific interest.¹ Their prolific occurrence under a sudden symmetry breaking transition and subsequent scaling behaviour are of universal character, finding parallels in areas as distant as cosmology and particle physics.² In this paper, we are concerned exclusively with singular line defects in the director field $\mathbf{n}(\mathbf{r})$ of a nematic, which are referred to as threads or disclinations. Two types of disclination are distinguished, namely, the wedge (or axial) and the twist (or perpendicular).³ The former variety is obtained when the flux lines of $\mathbf{n}(\mathbf{r})$ lie in planes orthogonal to the defect line, or the rotation vector Ω is parallel to the disclination. In the latter case, Ω is transverse to the line defect. Singular lines causing least distortion are of strength $s = \pm 1/2$, with $2\pi s$ being the angle by which the apolar unit vector \mathbf{n} rotates in circumnavigating the defect core. Topologically, rectilinear half-strength disclinations are all equivalent regardless of their polarity (\pm) and type (wedge/twist), and can be smoothly transformed into one another. Further, such defects cannot be eliminated through continuous director deformations and are topologically constrained either to end upon themselves forming closed loops, or to terminate at interfaces. They are among the experimentally realizable analogues of cosmic strings.

Half-strength disclination loops, our main theme here, may be of purely wedge or twist type, or of mixed character involving

both types. A pure wedge loop of given polarity possesses a net (global) topological charge, being in effect a $|s| = 1$ monopole, or a hedgehog, at distances large compared to its dimensions; in fact, the transformation between charged loops, either of pure wedge or mixed type, and point defects is a much researched subject;^{4–6} on the other hand, a twist loop (Fig. 1) causes no director gradients far away from it and, therefore, carries no net

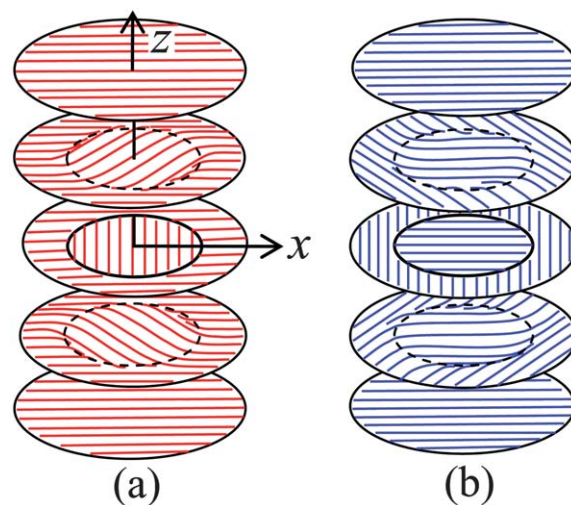


Fig. 1 Director field corresponding to a half-strength twist disclination loop separating π -twisted and untwisted regions of a nematic slab with planar boundary conditions. The director \mathbf{n} is continuous everywhere, given by $\mathbf{n} = (\cos \varphi, \sin \varphi, 0)$, except in the plane of the loop in which it changes abruptly across the line singularity. (a) Normal twist loop L(T) encircling the π -twisted inner domain. (b) Inverse twist loop L(P) encircling the untwisted inner domain.

^aCentre for Soft Matter Research, P. O. Box 1329, Jalahalli, Bangalore, 560013, India. E-mail: murthyksk@gmail.com

^bMartin-Luther-Universität Halle, Institut für Physikalische Chemie, von-Danckelmann-Platz 4, 06120 Halle (Saale), Germany

† Electronic supplementary information (ESI) available. See DOI: 10.1039/c1sm05245d

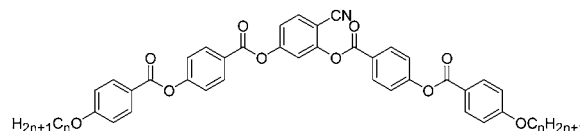
topological charge. While the theoretical advances on the energetics and stability of annular singularities have been quite remarkable, experimental exploration has not always kept pace with the predicted behaviour. In particular, the properties of pure twist loops analyzed very early by Friedel and de Gennes⁷ appear to have remained unexamined in the laboratory so far. These authors considered a nematic under torsion, with **n** along *x* at one of the substrates and along $-x$ at the other, and with the imposed twist across the sample being through π about the layer normal *z*. They envisaged the twist to relax by the nucleation of singular loops *L*(*P*) enclosing domains with uniform planar orientation along *x* (Fig. 1b), and predicted that such loops of circular geometry should exhibit a critical radius R_c separating the growth and decay regimes. It is our primary purpose here to describe experiments that demonstrate the realization of these theoretical results. A novel process of generating twist loops of varied sizes forms a significant part of this study. Our second objective concerns the dynamics of twist loops *L*(*T*) and *L*(*P*). For collapsing circular disclinations *L*(*T*), the balance between the elastic force, which is derived exclusively from the disclination energy, and the viscous force requires the radius *R* to vary as $(t_o - t)^{1/2}$, where t_o is the time at which the loop disappears completely; and this behaviour is also observed in some previous experiments.⁸ However, when the twist energy also enters the analysis, *R*(*t*) is expected⁹ to scale as $(t_o - t)^\alpha$ with α asymptotically approaching unity. In a previous experimental study on two polymer nematic solutions,¹⁰ the area of twist loops has been found to vary as $(t_o - t)^2$. For the compound studied here, we find α to vary with *R* just as expected. We also find that, for enlarging loops *L*(*P*), *R*(*t*) is nearly linear provided $R \gg R_c$. We have extended an earlier theoretical description of *L*(*T*) to the case of *L*(*P*) to fully account for the dynamics of both subcritical and supercritical loops. This analysis provides a simple method of extracting the related viscoelastic parameter. We also demonstrate the generality of our results on twist loops in a bent-core compound by our observations on a calamitic liquid crystal, presented as Electronic Supplementary Information (ESI).†

2 Experimental section

The sample cells used were sandwich type, constructed of passivated indium tin oxide (ITO) coated glass plates from Delta Technologies. The planar alignment was secured by spin coating the ITO electrodes with polyimide and then buffing unidirectionally the coated surfaces on a velvet cloth. The rubbing direction and the layer normal define the reference axes *x* and *z*, respectively. Mylar spacers, heat-sealed to the electrodes through cooling from $\sim 250^\circ\text{C}$ under a uniform pressure, determined the cell gap *d*, which was measured interferometrically. Optical observations were made using a Carl-Zeiss Axio Imager.M1m polarizing microscope equipped with an AxioCam MRc5 digital camera. The sample temperature *T* was maintained to an accuracy of $\pm 0.1^\circ\text{C}$ by an Instec HCS402 hot-stage connected to a STC200 temperature controller. The voltage source was a Stanford Research Systems DS345 function generator coupled to a FLC Electronics voltage amplifier (model A800). The cited rms values of the applied voltage $V(t) = \sqrt{2} V_{\text{rms}} \sin \omega t$ were measured with a Keithley-200 multimeter. For dielectric spectra, determined on a HP4194A Impedance/Gain-phase analyzer, the

cell voltage was 0.5 V and the samples were magnetically aligned using a field $B \approx 1.38\text{ T}$ from a Bruker B-MC1 electromagnet.

The material investigated, 4-cyanoresorcinol bis[4-(4-*n*-hexyloxybenzoyloxy)benzoate] (6OCN), belongs to the homologous series of compounds *n*OCN first synthesized by Kovalenko *et al.*¹¹



The observed phase sequence of 6OCN in the heating cycle is *Cr* 105 $^\circ\text{C}$ *N* 138.3 $^\circ\text{C}$ *I*, with *Cr*, *N* and *I* denoting respectively the crystal, nematic and isotropic phases. The *N* phase supercools to as low as 67 $^\circ\text{C}$ below which crystalline spherulites nucleate. All our experiments were performed at temperatures between 80 $^\circ\text{C}$ and 130 $^\circ\text{C}$. We use the reduced temperature $T_r = T/T_{\text{NI}}$, T_{NI} being the *N*-*I* transition temperature, in comparing different compounds *n*OCN.

3 Results and discussion

3.1 Dielectric and electroconvective responses

Before discussing the generation of twist loops, it is useful to first describe the typical frequency dependence of the electrical parameters and the instability characteristics for 6OCN at a chosen temperature. Fig. 2 illustrates these aspects for 120 $^\circ\text{C}$. The relaxation behaviour of the principal permittivities presented in Fig. 2a are very similar to those of 9OCN and 12OCN discussed in our earlier reports.^{12,13} The dielectric response along **n** is described by the complex permittivity function

$$\epsilon^* = \epsilon_2 + \frac{\epsilon_s - \epsilon_1}{1 + i\omega\tau_1} + \frac{\epsilon_1 - \epsilon_2}{1 + (i\omega\tau_2)^{1-\alpha}} - \frac{i\sigma_s}{\epsilon_o\omega} + \frac{a}{\omega^b}, \quad (1)$$

where ϵ_s is the static permittivity, σ_s the static conductivity, ϵ_i the frequency limit of the i^{th} mode, τ_i the relaxation time of the i^{th} mode, and α the Cole–Cole distribution parameter; *a* and *b* are adjustable parameters in the last term, which accounts for the contribution of the double layers to the real part of permittivity, ϵ' ; the previous term accounts for the conductivity contribution to the imaginary part, ϵ'' . This equation also describes $\epsilon_\perp^*(\omega)$, but with a single relaxation function of the Cole–Cole type. Evidently, the first of the longitudinal relaxations is a Debye like process; it is associated with the end-over-end rotations of the molecules around their short axes, which is severely retarded by the nematic potential. On the other hand, both the longitudinal and transverse relaxations occurring around a few MHz involve a Cole–Cole type mechanism; even in the isotropic phase, a similar relaxation is observed. These relaxations, characterized by a distribution of time constants, may arise due to independent rotations of dipolar groups around the long axis. In calamitics, the corresponding modes usually occur in the GHz region; their large down shift here is ascribable to the increased molecular size and very high viscosity of the medium. Interestingly, unlike in 9OCN or 12OCN, the dielectric anisotropy $\epsilon_a = (\epsilon_\parallel - \epsilon_\perp)$ of 6OCN remains positive till the dielectric sign reversal frequency $f_i \approx 45\text{ kHz}$. The ratio of principal electrical conductivities

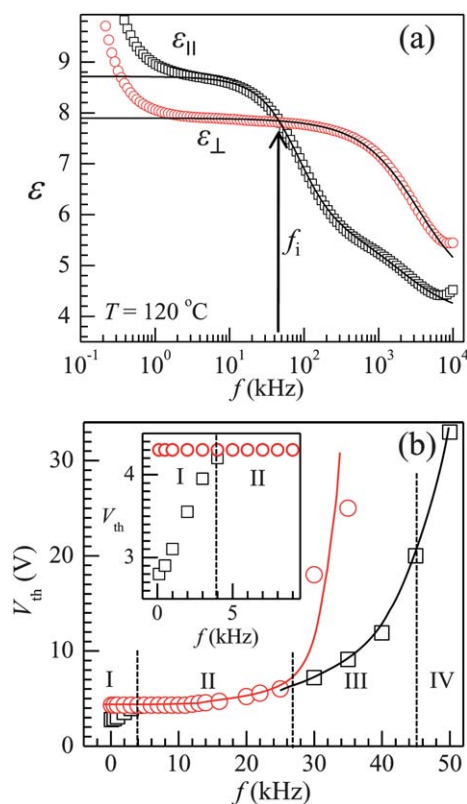


Fig. 2 (a) Frequency dependence of the real part of complex dielectric permittivity ϵ^* measured along (\parallel) and transverse (\perp) to the nematic director. The continuous lines are the fits to eqn (1). (b) Frequency dependence of the threshold voltage $V_{th} = V_F$ for the Fredericksz effect and/or $V_{th} = V_C$ for electroconvection (EC) in 6OCN at 120 °C. Inset is an enlarged view of region I. In regions I and III, the primary bifurcation is to the EC state from which the Fredericksz state evolves at a higher voltage. The only instability observed in region II is the Fredericksz effect, and that in region IV, EC.

$\sigma_{\parallel}/\sigma_{\perp}$ is ~ 1.36 at low frequencies; the conductivity anisotropy $\sigma_a = (\sigma_{\parallel} - \sigma_{\perp})$ is positive at all frequencies upto ~ 0.7 MHz above which it turns negative.

The phase diagram of 6OCN in Fig. 2b reveals an interplay between the Fredericksz effect and electroconvection (EC) that is consistent with the variations $\epsilon(f)$ and $\sigma(f)$. Under an increasing f below 4 kHz (region I, Fig. 2b), the compound undergoes primary bifurcation from the planar base state into the standard EC state at a critical voltage V_C involving, besides the various anisotropic elastic, hydrodynamic and electrical parameters of the material, the critical wave vector $\mathbf{k} = (q, p)$ appropriate to a given f (for details, see eqn (3.11), ref. 14); V_C is an increasing function of f .³ Fredericksz state sets in at a higher threshold $V_F = \pi\sqrt{(k_{11}/\epsilon_0\epsilon_a)}$, where k_{11} is the splay elastic constant; V_F remains constant till ~ 11 kHz, and is greater than V_C below the codimension-2 (C2) point corresponding to the crossover of the two bifurcation lines (Fig. 2b, inset). Beyond the C2 frequency of ~ 4 kHz and up to ~ 26 kHz (region II, Fig. 2b), only the Fredericksz state is found stable since $V_C > V_F$. However, with further increase in f , in region III, V_C is again lower than V_F due to the low frequency relaxation of ϵ_{\parallel} and consequent monotonic decrease in ϵ_a ; thus, in this region, EC which reoccurs as the

primary instability is followed by dielectric reorientation at a diverging threshold. In region IV, wherein the planar sample is dielectrically stable, only EC is observed. Regions I–IV are found in different frequency intervals for different temperatures $T > 110$ °C. For instance, the upper frequency limits of regions I, II, and III are, respectively, 1, 11 and 25 kHz at 110 °C; 1.1, 18 and 32 kHz at 115 °C; and 2.1, 104, and 156 kHz at 130 °C. Region II decreases in width with lowering T and ceases to appear for $T < 100$ °C.

3.2 Generation of twist disclination loops

We begin with a description of three representative experimental scenarios in which a structural twist develops in an initially planar nematic layer, and then proceed to present a model of the director fields that would account for the observations. The first of these is presented in Fig. 3a, b. These textures, which belong to region II of the phase diagram where the sample is unstable against Fredericksz effect but stable against EC, are obtained as follows. The sample is suddenly exposed to a large potential of about $3V_F$. This creates a large number of Brochard-Leger^{15–17} walls that bridge energetically degenerate contiguous regions of equal and opposite tilts. Under the high electric field, the walls are so narrow as to involve a large distortion energy that is relieved through the process of ‘pincement’ or transformation of a wall into a pair of oppositely charged wedge disclinations of strength $|s| = 1/2$.^{3,18} In Fig. 3a, we see, in the field on state, a part of two closed singular lines resulting from the pincement of a closed irregular wall. It is important to observe here that they are separated laterally along both x and y , implying a differential speed of collapse for the two loops. The same region appears as in Fig. 3b soon after switching the field off, when the relaxation to the base state is still incomplete; in the region of separation between the earlier line singularities, where a dark-green interference colour is seen, the half-turn structural twist is developing; the two insets, recorded a few seconds apart after the birefringence colours in the twisted (bright green) and untwisted (dark green) regions became steady, show the tendency of the twisted domain to become circular. The existence of π -twist in the bright green islands is inferable from the disposition of the Williams rolls, as will be seen later. The second situation leading to twisted domains is depicted in the serial images in Fig. 3c–f recorded in the Fredericksz state of region I. In Fig. 3c, showing the wall state immediately before the onset of pincement, the closed and open walls have come in contact. In Fig. 3d, the pincement has begun at the contact point with one of the singular lines being common to both the walls. In Fig. 3e, the pincement is almost complete and the closed singular loop is rapidly shrinking. The texture in Fig. 3f recorded after field removal shows a bright green island where the director is twisted through π between the substrates. The third scenario in the twisting process is presented in Fig. 3g, h. The pattern in Fig. 3g shows a hybrid disclination loop anchored at two dust particles along a wall. The pincement leading to the loop nucleated at the wall–disclination coexistence point to the right and propagated till reaching the dust particle to the left. On removal of the field, the region within this loop gets π -twisted, as seen in Fig. 3h.

The director field associated with a twist disclination loop is revealed by the EC pattern obtained on subjecting the sample

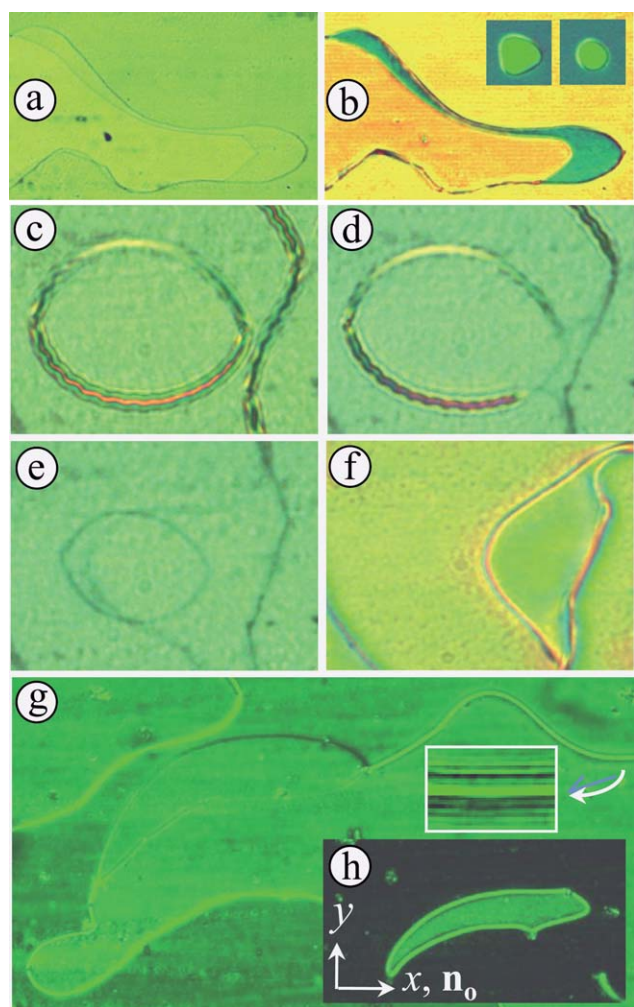


Fig. 3 Typical processes by which a twist disclination loop evolves around a π -twisted region. Crossed polarizers set diagonally in (a–g), and along x , y in (h); 120 °C. (a) Disclination lines from pincement of a wall showing lateral relative shift along x and y ; 15 V, 10 kHz. (b) Same region as in (a) soon after switching the field off; the greenish region is in the process of developing a π -twist; the insets, recorded a few seconds apart after the birefringence colours in the twisted (bright green) and untwisted (dark green) regions became steady, show the tendency of the twisted domain to become circular. (c)–(f) Time series with (c)–(e) in the field on state ($f = 1$ kHz, $V = 14$ V) and (f) after field removal: (c) A closed wall in the vicinity of a zig-zag wall prior to pincement; (d) pincement originating at the contiguous parts of the two walls with one of the line defects common to both walls; (e) complete transformation of the walls into singular lines; (f) after the disappearance of the closed disclination, a π -twisted domain with greenish birefringence colour remains; it is surrounded by a planar yellow-green region. (g) A hybrid disclination loop anchored at two dust particles along a wall; the pincement leading to the loop nucleated at the dust particle to the right and propagated till reaching the particle to the left; inset shows the interference fringes in the wall region; (h) twist loop formed within a planar region in the off-state.

containing the loop to a potential slightly above V_C in either of the frequency regions I or III of Fig. 2b. Fig. 4a shows a typical pattern seen in this situation when the chosen frequency lies above the Lifshitz point f_L ; it is well established that the primary bifurcation is to a state of oblique rolls for $f < f_L$, and normal rolls for $f > f_L$.¹⁴ The pattern in Fig. 4a shows the conventional

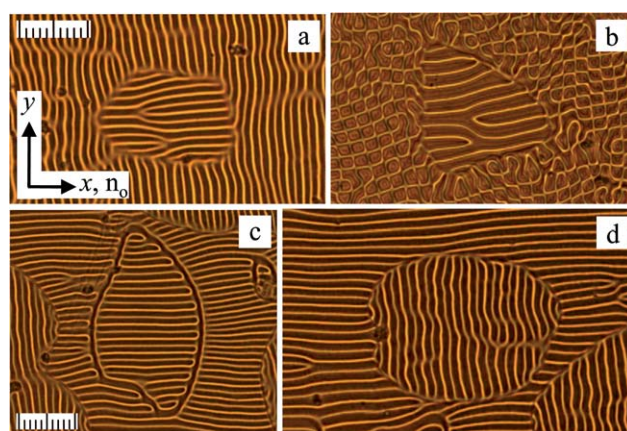


Fig. 4 Electroconvection patterns of the conduction regime enabling identification of the planar and π -twisted regions. Single polarizer along x . (a) Rolls normal to \mathbf{n}_0 in the inner π -twisted and surrounding planar domains separated by a $|s| = 1/2$ twist line (normal loop); 20 kHz, 9.5 V, 115 °C. (b) Bimodal (square grid) pattern in the planar region enveloping the π -twisted normal roll domain; 100 Hz, 4 V, 120 °C. (c) Central domain delimited predominantly by a $|s| = 1$ twist disclination separating reverse π -twisted regions; 20 kHz, 9 V, 115 °C. (d) Rolls normal to \mathbf{n}_0 in the inner planar and surrounding π -twisted domains separated by a $|s| = 1/2$ twist line (inverse loop); 20 kHz, 9 V, 115 °C.

normal rolls with their wavevector along x in the area surrounding the inner domain. The Carr-Helfrich mechanism^{14,19} that drives this instability relies essentially on the coupling between σ_a and the bend-type curvature fluctuations in the sample. In a planar nematic layer, when $\varepsilon_a < 0$ (or slightly positive) and $\sigma_a > 0$, this coupling leads to the formation of periodic space charges of alternating sign along the initial director \mathbf{n}_0 . The body force on these charges sets up periodic cellular flows above a critical voltage V_C determined by the balance between hydrodynamic, dielectric and elastic torques. Thus, the Carr-Helfrich mechanism stabilizes the periodic stationary director modulation along \mathbf{n}_0 , in the xz plane defined by the applied field and \mathbf{n}_0 . At threshold, this modulation is mostly confined to the sample midplane. The focusing action of this periodic director field for the extraordinary rays vibrating along x produces line images normal to \mathbf{n}_0 , as seen in the outer region in Fig. 4a. Similar considerations also apply to the central domain in Fig. 4a, where the focal lines are along x . We may recall here that, in travelling through a twisted structure, an incident light vector vibrating along x or y adiabatically follows the twist as long as the Mauguin condition,³ i.e., $\Delta n P \gg 2\lambda$ with Δn as the birefringence, P as the pitch and λ as the wavelength, is satisfied. For 6OCN, $\Delta n = 0.169$ at 120 °C and 0.546 nm, so that this condition is approximately met in π -twisted layers of thickness 8–12 μm that we used. Thus the incident light linearly polarized along x remains almost linear along the local director in a π -twisted layer; when the normal roll instability is excited in the layer, the light vibrating along y in the sample midplane experiences periodic refractive index modulations due to the distortions therein, and gets focused into line images along x . We may, therefore, surmise the structure in the inner domain of Fig. 4a as π -twisted. Since the alignment in the surrounding region is planar, there must exist a $1/2$ strength twist singularity delimiting the central domain.²⁰ The EC threshold for the twisted

state, compared to the planar state, is slightly higher, and also the sequences of secondary instabilities differ for the two states. Accordingly, the texture for $f < f_L$ in Fig. 4b shows a secondary structure (bimodal) involving two nearly orthogonal wave vectors in the planar region, and a one dimensional structure in the twisted region. Fig. 4c reveals the formation of oppositely twisted contiguous regions with a separating $|s| = 1$ line. The pattern of rolls in Fig. 4d reveals the formation of an inverse twist loop around the central planar domain. In passing, we may note that the inplane director rotation in a Mauguin twisted domain is often directly detectable through conoscopic observations,³ even when the adiabatic theorem precludes its detection in parallel light. The equilateral hyperbolae of the conoscopic figure rotate relative to their orientation in the untwisted sample by half the angle of total twist. However, because of the 4-fold axis of the conoscopic figure, this rotation is not revealed in a half-turn twisted sample.

Pincement of walls, which is a common feature in the different scenarios illustrated in Fig. 3, is the basis for the novel procedure we have employed to generate the π -twisted domains within planar surroundings and *vice versa*. In an attempt to analyse how the separation of wedge lines may bring about the twist, we now examine the director patterns in the field on state at different levels of excitation with reference to the schematic illustration in Fig. 5. Irregularly shaped closed walls, as they collapse with time, are predicted to approach an equilibrium elliptical geometry with the major axis along \mathbf{n}_0 being $\sqrt{(k_{33}/k_{22})}$ times the minor axis;¹⁵ here, k_{33} and k_{22} are the bend and twist elastic constants, respectively. Fig. 5a shows the director field in the mid plane of an elliptical wall that is splay-bend (SB) type at A and C (Fig. 5b), and twist-bend (TB) type at B and D (Fig. 5e). At $\sim 2.2 V_F$, the wall narrows greatly, involving too large a curvature strain for it to be stable against pincement.^{3,18} It has been shown²¹ that the voltage V_E at which a straight, initially planar wall and the pair of disclination lines due to it are in equilibrium is given by

$$\frac{V_E}{V_F} = \sqrt{2} \beta \ln \left(\frac{dV_F}{\pi \zeta V_E} \right) \quad (2)$$

Here, ζ is of the order of the nematic correlation length, ~ 6 nm, and the factor β varies between $1/4$ and $1/2$ depending, respectively, on whether the disclination is isolated from the boundary or adhering to it. Experimentally, we found $V_E \approx 2.2 V_F$ in a $8 \mu\text{m}$ thick sample, and this corresponds to $\beta \approx 1/3.4$. While the wall state is favoured for $V_F < V < V_E$, the disclination state is favoured for $V > V_E$. However, even above V_E , pincement requires nucleation; it originates usually at impurities attached to the wall or on contact of the wall with an outside disclination. The director fields in the SB and TB regions of a pinched loop wall may broadly be depicted as in Fig. 5c and 5f, respectively.

The disclination loops L_t and L_b formed respectively near the top and bottom substrates (Fig. 5c and 5f), notably, are without any net topological charge; in each case, the wedge lines at A and C are of opposite strength; and so are the twist lines at B and D for which the rotational vectors are opposite. Ideally, these loops collapse in the layer plane, along the local radii of curvature. However, the collapse rates for L_t and L_b are generally not the same along a given direction, and this dynamical symmetry breaking is particularly evident for the

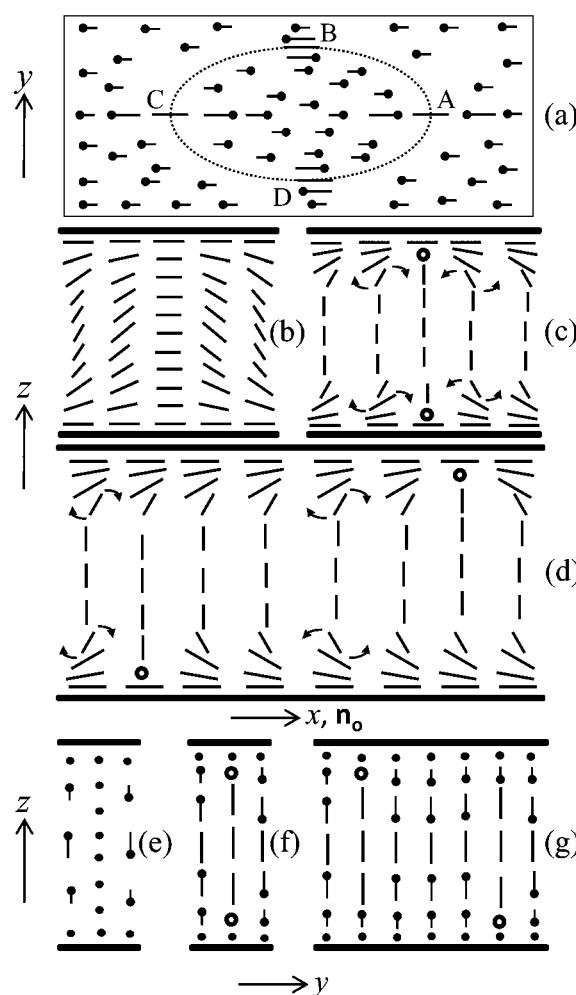


Fig. 5 Director fields in the wall and disclination states. (a) Midplane field for a Brochard-Leger loop wall. Pins indicate out-of-plane tilts with their heads above the plane of the figure. The distortion type is splay-bend (SB) at A and C, and twist-bend (TB) at B and D. (b) SB section of the wall at A as seen along y . (c) Same section as in (b) after transformation of the wall into wedge disclinations of strength $+1/2$ (top circle) and $-1/2$ (bottom circle). (d) The changed field after the disclinations in (c) undergo a relative lateral shift; curved arrows in (c) and (d) indicate the local elastic torques under which relaxation to the base state occurs on switching off the field. (e) TB section of the wall at B as seen along x . (f) Same section as in (e) after transformation of the wall into two half-strength twist disclinations. (g) The changed field after the disclinations in (f) undergo a relative lateral shift. The sections (b) and (e), on rotation by 180° about x and y respectively, give the corresponding sections at C and D.

corresponding wedge disclinations forming at A, or C, in Fig. 5a. The lateral shift thus produced is of crucial importance to the production of twist loops. As a rule, after field removal, the sample volume corresponding to the area common to L_t and L_b in the planform returns directly to the planar state; and that corresponding to nonoverlapping parts, between L_t and L_b , acquire a π -twist (see, for example Fig. 3b). The reason for these differing relaxational modes becomes clear, for example, by a comparison of the director field in Fig. 5c with that in Fig. 5d. In Fig. 5c, where there is no lateral shift between the disclinations, the elastic torques in both upper and lower

halves, on either side of the yz plane containing the defects, has the same sense. Therefore, the planar realignment progresses without any conflict of torques in the midplane region, and the line defects move toward each other toward final annihilation. On the other hand, in Fig. 5d, which gives the \mathbf{n} -field for the laterally shifted wedge disclinations initially formed at A, the field in the region, say Σ , between the yz planes containing the defect lines (locally along y) has opposite elastic torques in the upper and lower halves. It resembles the Freedericksz texture of a nematic in an inverse pretilt cell that is apt to relax to the intermediate half-turn twisted texture on field removal.²² On either side of the Σ region, the situation in Fig. 5d is just as in Fig. 5c, favouring a direct transition to the planar state. These considerations apply equally to the relaxation process in the region of twist disclinations, as a comparison of Fig. 5g with Fig. 5f would show. In the process of relaxation, as a topological necessity, the laterally displaced disclinations move to the midplane and eventually transform into a twist loop between the twisted and untwisted regions (Fig. 1). The progressive disappearance of the out-of-plane director tilt that occurs during the transient will involve different rotation vectors in different regions. For example, in Fig. 5d, the rotation vectors within Σ are \mathbf{x} (or, equivalently, $-\mathbf{x}$) in the midplane, both \mathbf{x} (or $-\mathbf{x}$) and \mathbf{y} in the upper half, and both \mathbf{x} (or $-\mathbf{x}$) and $-\mathbf{y}$ in the lower half; outside Σ , the rotation vectors are \mathbf{y} to the left and $-\mathbf{y}$ to the right. Essentially, therefore, the differential rate of lateral movement of the disclination lines is at the root of the development of twist. Movement of a line defect may be affected due to external influences; the line, for example, may be stuck at a dust particle indefinitely. More fundamentally, anisotropic line tension, determined in turn by anisotropic elasticity, may influence the relative rates of disclinations of different types. While the configuration of a $-1/2$ wedge disclination is only marginally influenced by the splay bend anisotropy $k_a = (k_{11} - k_{33}) / (k_{11} + k_{33})$, that of a $+1/2$ wedge disclination changes strongly with k_a , from pure splay for $k_a = -1$ to pure bend for $k_a = +1$. In ordinary calamitics, having $k_{33} > k_{11} > k_{22}$, we may therefore expect the line tension for a $-1/2$ wedge line that is rich in bend to be greater than that for a $+1/2$ wedge line that is rich in splay.²³ This has indeed been observed to be the case experimentally.²⁴ For 9OCN, we find $k_{33} < k_{11}$ in the entire nematic range, and k_{11} for 6OCN comparable to that in 9OCN at the same reduced temperature.¹³ Thus, the $+1/2$ line is likely to be bend rich in these compounds, although, since k_{11} is finite, it may not comprise the bend exclusively. Regardless of the sign of k_a , as earlier perturbative calculations show, the $-1/2$ line possesses more energy relative to the $+1/2$ line, the excess energy being proportional to k_a^2 .²³ We may thus expect the $-1/2$ line to be always faster driven.

We need to clarify here that the director patterns for higher fields in Fig. 5 are over simplified to facilitate the explanation of the twisting mechanism. It is known, for instance, that at elevated fields the splay-bend deformation at each of the extremities of the major axis of an elliptical loop wall is relaxed by a more complex but less energetic structure, which is mostly twist.²⁵ Since twist can be either left- or right-handed, and has to match with the twist deformations along the minor axis, both chiralities appear in the wall, separated by a twist disclination of

unit strength. The director escape out of the xz plane in the SB region, recognizable by the appearance of interference colours under crossed polarizers with their axes along and transverse to the wall, is known to begin at $\sim 2V_F$.²¹ In fact, it is the azimuthal director deviation that, during relaxation in the field off state, produces the flow velocity component along y , which in turn initiates the director twist in the sample midregion under suitable boundary conditions.

In the foregoing description, we have focused on the ‘normal’ twist loops L(T) (Fig. 1a). In order to produce inverse twist loops L(P) (Fig. 1b), we raise the voltage in the Freedericksz state in any of the regions I–III (Fig. 2b) to be far above V_F . The complex motion of various disclination lines often produces a few smaller disclination loops completely enclosed within larger loops. On removal of the field, the region immediately surrounding the smaller loops becomes π -twisted. Within the smaller domains, the original planar alignment is usually recovered. Sometimes a π -twist that is of opposite sense compared to outside may develop inside a smaller loop; then a $|s| = 1$ disclination loop separates the reverse twisted regions. These features are illustrated in Fig. 6 showing the textures obtained in region III of the phase diagram (Fig. 2b). Relaxation from a highly entangled disclination state may also produce a variety of twist lines involving both half-turn and full-turn chiral domains, as seen in Fig. 7. Here, our identification of 2π -twisted regions is based on their faster decay rate ($4\text{--}5 \mu\text{m s}^{-1}$) compared to π -twisted regions ($<1 \mu\text{m s}^{-1}$). Interestingly, the planar and 2π -twisted regions appear to be separated by two $s = 1/2$ line defects instead of a single $s = 1$ line as envisaged in an early study,²⁰ since the disclination energy is known³ to vary as s^2 , this is understandable provided the director escape in the $s = 1$ configuration does not offset the difference in energy.

3.3 Stability and structure of circular twist disclination loops

The structure and energy of a nematic layer anchored planarly at the bounding plates and containing a single circular loop thread, as in Fig. 1a, was first analyzed in detail by Nehring,²⁰ assuming the fluid as elastically isotropic ($k_{11} = k_{22} = k_{33} = k$). The Frank free energy for this case is given by the volume integral $E = \frac{k}{2} \int (\nabla\phi)^2 d\tau$, the minimization of which requires $\nabla^2\phi = 0$. In the long thread limit $R \gg d$, and when the core circumference $2\pi c \ll d$, the total energy is expressible as

$$E = E_o + \frac{\pi^2 k}{2} \left[\frac{\pi R^2}{d} + R \ln \frac{d}{4\pi c} + R \ln \left(\sec \frac{\pi b}{d} \right) \right] \quad (3)$$

Here E_o denotes the energy of the tubular core of radius c ; the first term in square brackets is the energy due to the uniform twist in the inner cylindrical domain of radius R , and the other two terms represent the strain energy associated with the loop thread located in the xy plane at a distance b from the midplane. With decreasing R , the total free energy reduces monotonically, rendering the loop unstable toward collapse regardless of its size. It is also shown²⁰ that the equilibrium position of the loop corresponds to $b = 0$ for which the last term in braces in eqn (3) vanishes. Thus, taking e_o to be the core energy per unit length, the overall energy per unit length E_L for a loop in the equilibrium position is

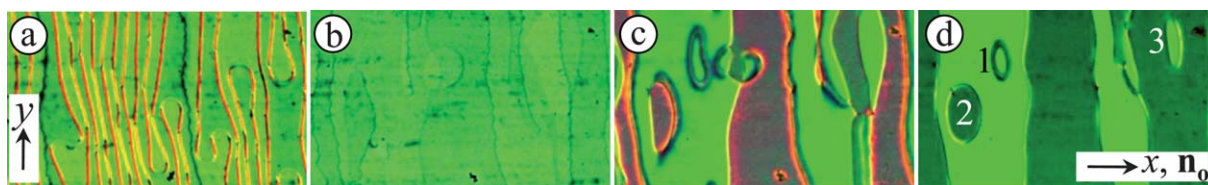


Fig. 6 Generation of annular twist disclinations of different types. (a–d) Textures of the same region between diagonally crossed polarizers at 120 °C. (a) Longish loop walls undergoing pincement at 30 kHz, 40 V; after exciting the normal roll instability at a low voltage in regime III of Fig. 2b, the voltage is increased here to $\sim 5V_F$. (b) Disclination state at 60 V. (c) Texture obtained soon after field removal, during the decay time; the green regions are twisted and the brown regions are in the process of regaining the planar alignment. (d) Texture at the end of relaxation, exhibiting (1) $|s| = 1$ loop between reverse twisted regions, (2) $|s| = 1/2$ inverse twist loop and (3) $|s| = 1/2$ normal twist loop.

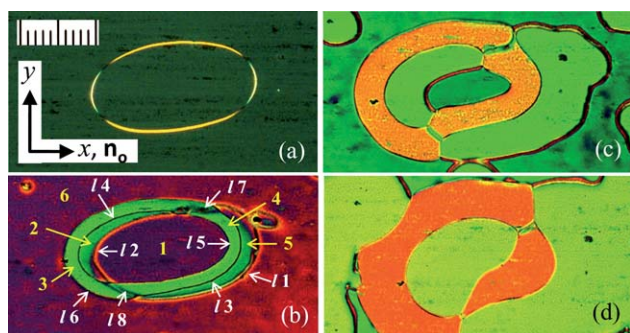


Fig. 7 Formation of a variety of twist disclinations in the fluid relaxing from a very high field. Diagonally crossed polarizers, 120 °C. (a) Highly narrowed elliptical wall in the quasihomoeotropic splay Freedericksz state at 100 V ($\approx 20 V_F$), 10 kHz, just before its transformation into $\pm 1/2$ disclinations; line defects already formed are masked in the dark background. (b–d) Time images during the relaxation process: (b) Birefringent regions (1–6) with demarcating line defects (11–18), immediately after field removal. (c) Texture of changed interference colours 10 s after (b); the blue-green regions 1 and 6 are 2π twisted; yellow regions 3 and 4 are π twisted; and green regions 2 and 5 are planar. Regions 2–5 are growing at the expense of 1 and 6. The line 11, as well as 12, is composed of two $1/2$ -strength twist lines separating the planar and full-turn regions. Lines 13 and 14 are the common $1/2$ -strength twist lines separating the planar and half-turn regions. Lines 15 and 16 are seemingly $1/2$ -strength twist lines separating the full-turn and half-turn regions of like handedness. Lines 17 and 18 are $s = 1$ twist lines between oppositely twisted regions 3 and 4, which makes the twists in regions 1 and 6 opposite. (d) Decaying π twisted regions within the planar sample in the final stages of relaxation, 15 s after (c). 5 μm scale div.

$$E_L = e_o + \frac{\pi k}{4} \left[\frac{\pi R}{d} + \ln \frac{d}{4\pi c} \right] \quad (4)$$

Consequently, the force per unit length $-dE_L/dR$ remains constant and roughly equal to the viscous drag force $\eta(dR/dt)$, so that R may be expected to vary as $(t_o - t)$, where t_o is the time of annihilation; the proportionality constant includes the effective viscosity η , k and d . This prediction may be compared with that in some earlier studies on the dynamics of half-strength disclinations,^{8,26,27} wherein the energy per unit length is taken merely as $E_L = e_o + (\pi k/4) \ln(R/c)$; then, on equating the viscous dissipation force $-\eta(dR/dt)$ with the gradient of energy dE_L/dR (or with E_L/R under the logarithmic approximation of constancy of E_L) and integrating, we are led to R varying as $(t_o - t)^{1/2}$. Various experiments^{8,26–29} on coarsening dynamics of line defects that confirm the scaling exponent in $R \propto (t_o - t)^\alpha$ to be close to $1/2$

do not describe the structure of the disclination loops investigated. However, in some studies¹⁰ dealing specifically with $1/2$ strength twist loops in nematic solutions of rodlike polymers, area $A(t)$ of the loops, as earlier noted, is found to relax as $(t_o - t)^2$ in the long thread limit. In a detailed mathematical description of loop dynamics, Sonnet and Virga⁹ have evaluated $R(t)$ by balancing the rate of gain in total elastic free energy due to loop shrinkage against the rate of total dissipation due to the viscous torque, and analyzed the dependence of α on the dimensionless parameter $r = D/d$, D being the loop diameter.

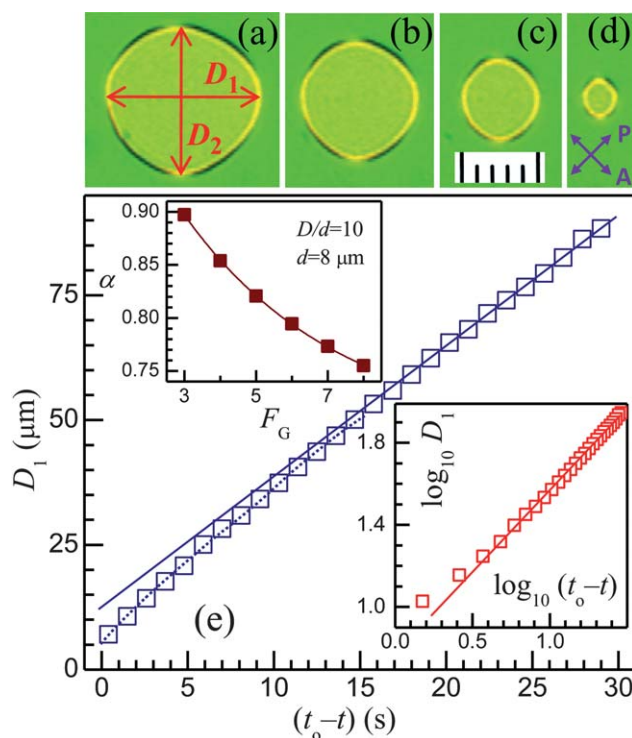


Fig. 8 (a–d) Time photographs of a collapsing disclination loop of strength $1/2$ separating the inner half-turn twisted region from the surrounding untwisted region. 4.4 s between successive frames. Diagonally crossed polarizers (P, A). The interference colour within the loop differs from that outside since the Mauguin condition for adiabatic wave guidance is not fully met. 120 °C, 5 μm scale division. (e) Loop diameter D_1 as a function of time $(t_o - t)$ remaining for annihilation, showing accelerated motion close to t_o and near linearity at the start. Lower inset: Bilogarithmic plot giving the initial slope as ~ 0.8 . Upper inset: Scaling exponent as a function of the geometrical parameter F_G .

We may now discuss our experimental data on the dynamics of loops $L(T)$ in the light of the foregoing models. Fig. 8a–d shows a few representative time images of a collapsing near circular loop with D_1 and D_2 as the principal dimensions. In Fig. 8e depicting the time dependence of D_1 , it is evident that, as we approach annihilation through the regime $0 < D < 5d$, the motion tends to perceptibly accelerate. For $D/d > 5$, we do find a near linear variation as deduced using eqn (4), but the linearity is not perfect. As the bilogarithmic plot in the lower inset of Fig. 8e indicates, the slope of the line through the initial few points, or the scaling exponent α , is *ca.* 0.8. The reason for the slight nonlinearity becomes clear if we use, instead of the approximate eqn (4), the more accurate expression due to Sonnet and Virga,⁹

$$\frac{t_0 - t}{\tau} = a_2 r - (a_1 a_2 - a_3) \ln \left(1 + \frac{r}{a_1} \right), \quad (5)$$

where, as defined in eqn (13) of Appx. A, the coefficients a_i are determined by a geometrical parameter F_G involving c and d , and τ is the relaxation time dependent on the rotational viscosity γ_1 and k . The exponent α may be obtained from eqn (5) using $1/\alpha = [r/t(r)](dt/dr)$. It turns out that even when D is two orders greater than d , for reasonable values of F_G , α remains around 0.9, and approaches complete linearity only asymptotically. We have shown in Fig. 8 (upper inset) the dependence of α on F_G , assuming $D = 10d$, corresponding to the maximum loop diameter realized experimentally for a near circular loop. With $c = 10$ nm, which seems reasonable for a bent-core system, and $d = 8$ μm , we find $F_G = 6.64$. The corresponding $\alpha \approx 0.78$ compares reasonably with the observed exponent of 0.8 at $D_1/d = 10$. The value of γ_1/k at 120 °C, for the same core radius, is found using experimental (t, r) in eqn (5) to be ~ 63 ms μm^{-2} . The shrinking along D_2 follows the same pattern as that along D_1 .

We may now consider the stability of inverse twist loops $L(P)$ of circular geometry (Fig. 1b) from the view point of Friedel and de Gennes.^{3,7} They compared such a loop to a circular current carrying conductor, with the topological strength analogous to the current strength and the divergenceless gradient $\nabla\phi$ analogous to the magnetic field linked to the current element. They concluded the net increase in energy due to the presence of the $1/2$ strength loop to be

$$E = \frac{\pi k}{8} (L - 4qA) = \frac{\pi^2 k}{2} [R \ln(R/c) - qR^2], \quad (6)$$

where $L = 4\pi R \ln(R/c)$ is the self inductance of the loop,³⁰ $A = \pi R^2$ is the cross sectional area of the untwisted region and q is the twist per unit thickness. Recognizing that the negative term here refers to the excess energy of the planar domain over that of an equivalent twisted domain outside the loop, this energy expression is the same as eqn (3), except for the argument of the logarithm. Notwithstanding minor differences in the expressions for E in different reports,^{3,7,8,31} E is expected in every case to exhibit a maximum at a critical radius R_c , provided q and s are of the same sign. Loops with opposite s and q cannot in fact form.²³ From eqn (6), R_c is determined by the condition

$$R_c = \frac{1}{2q} \left(1 + \ln \frac{R_c}{c} \right) \quad (7)$$

The energy reduces on either side of R_c so that loops with $R < R_c$ are expected to shrink and vanish, and those with $R > R_c$, to

enlarge monotonically. In other words, in an enlarging loop above R_c , the rate of increase in strain energy of the line is more than compensated by the rate of decrease in twist energy; similarly, in a shrinking loop below R_c , the rate of decrease in strain energy of the line exceeds the rate of increase in the twist energy. Our observations clearly demonstrate the existence of the critical size. For illustration, we may compare the textures in Fig. 9a–c; the time images here show several half-strength twist disclination loops $L(P)$ of near circular geometry in different dynamical states. Loops 1, 2 and 8 are enlarging, while 3 and 4 are collapsing; loops 5 and 6 are shrinking very slowly; and loop 7 is enlarging very slowly. The changed birefringence colour (light green) in the twisted region, compared to that in the untwisted region (dark-green) as seen under diagonally crossed polarizers is due to the Mauguin wave-guide condition, which is, firstly, less adequately satisfied at any wavelength and, secondly, differentially satisfied for different wavelengths because of dispersion of birefringence. Coming to the value of the critical radius in our experiments, for a sample of given thickness, we find it to be temperature dependent. Fig. 10, for a 12.1 μm sample, shows $R_c(T)$ to be an increasing function that is almost linear; in the temperature range 80–130 °C, $R_c d$ varies between 1.25 and 1.8. The value of R_c expected from eqn (7) is close to this range. To be

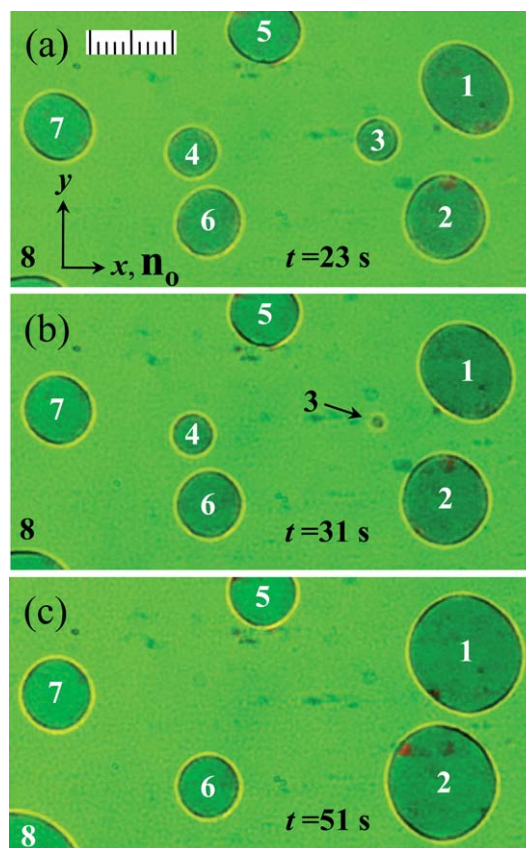


Fig. 9 (a–c) Several half-strength twist disclination loops between planar and surrounding π -twisted regions in different dynamical states at times t after removal of the field. Loops 1, 2 and 8 are enlarging, while 3 and 4 are collapsing; loops 5 and 6 are collapsing very slowly; and loop 7 is expanding quasistatically. Diagonally crossed polarizers. 130 °C. $d = 12.1$ μm . 5 μm scale div.

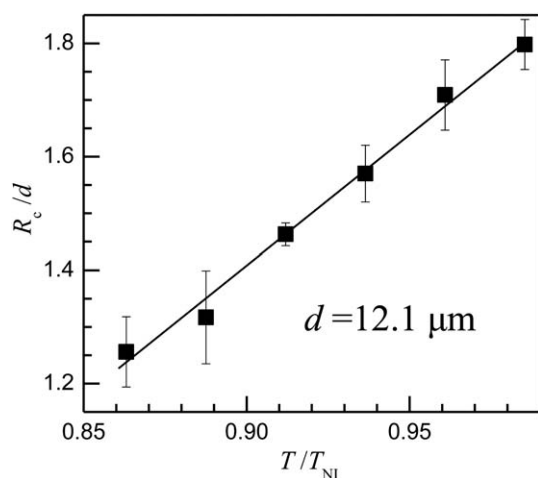


Fig. 10 Critical radius in units of sample thickness as a function of the reduced temperature.

specific, for a core radius of 10 nm and $d = 12.1 \mu\text{m}$, R_c/d should be about 1.33. Of the various static models,^{3,7,9,20,31} that of Sonnet and Virga,⁹ provides the best agreement with the experimental critical radius, as will be seen later. However, each of the models predicts some constant R_c for a given sample thickness regardless of temperature and, therefore fails to explain the variation $R_c(T)$ in Fig. 10. It may be possible to resolve this apparent anomaly by considering elastic anisotropy which is neglected in the various theories developed so far. Twist disclinations involve all the three Frank constants corresponding to splay, twist and bend deformations. As earlier noted, well below T_{NI} , k_{11} is considerably greater than k_{33} in 9OCN; for example, $k_{11}/k_{33} \approx 4$ at $T_r = 0.96$; our preliminary results indicate the same trend in 6OCN. Further, k_{33}/k_{22} for 6OCN, estimated from the ellipticity of Brochard-Leger walls, is ~ 1.6 in the temperature range 110–130 °C. If we associate the second term in eqn (6) with k_{22} and the first one with some k_{eff} involving both k_{11} and k_{33} , the predicted critical radius would depend on the factor k_{eff}/k_{22} . The experimental finding in Fig. 10 implies that this factor is an increasing function of temperature.

The time variation of loop diameter for both shrinking and enlarging loops L(P) is generally of the type presented in Fig. 11 for 130 °C. R_c is determined to be about 21.8 μm at this temperature. The change in the size of loops having their radii close to R_c is quasistatic over several seconds; loops with $R < R_c$ collapse at an ever increasing rate till annihilation. The growth of the loops with $R > R_c$, which is accelerated in the beginning, tends to reach a steady rate in the long thread regime. For shrinking loops time of annihilation serves as a convenient reference point. For enlarging loops, though the initial time is arbitrary, the growth rate is uniquely linked to the change in radius ($R - R_c$). Thus, in Fig. 11, the dotted line representing the growth of a single loop shows the same trend as the combined data for loops 2, 7 and 8 for which the initial times are suitably shifted to match the diameters. The dynamics of inverse disclination loops L(P) does not appear to have been analysed theoretically so far. However, the model of Sonnet and Virga⁹ for normal loops L(T) can be applied to the case of L(P) as well, as elaborated in Appendix A. It is readily seen from eqn (12) of the

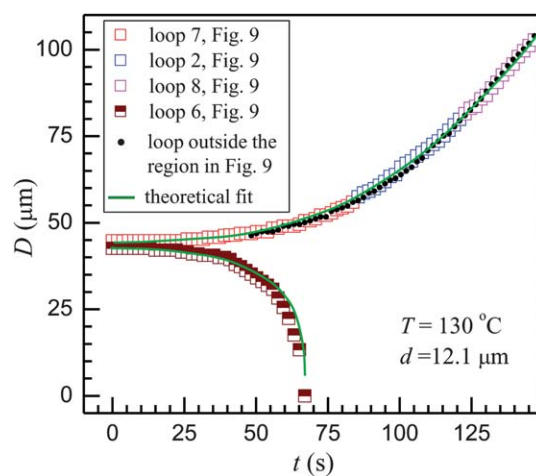


Fig. 11 Time dependence of diameter for shrinking and enlarging circular twist loops L(P). The critical radius R_c is about 21.8 μm . Loops with their radii close to R_c begin to move quasistatically; loops with $R < R_c$ collapse at an ever increasing rate till annihilation; those with $R > R_c$, which begin to grow at increasing rate, finally tend to reach a constant rate in the long thread regime. $t = 0$ corresponds to the time when loop 7 became perfectly circular. For the other enlarging circular loops, time scales are staggered to match their diameters. The dotted line, which is for a separate single loop, shows the same trend as the combined data for loops 2, 7 and 8.

Appendix that the loop radius becomes time independent for $r = r_c = a_1$ so that the critical diameter $2R_c = a_1 d$. The observed R_c of 21.8 μm in a 12.1 μm thick sample, corresponds to $a_1 = 3.6$ or, equivalently, $c = 9.453 \text{ nm}$. Supercritical loops with $r > a_1$ enlarge with time at an ever increasing velocity that reaches a terminal value of $1/a_2\tau$ corresponding to $r = \infty$. Surprisingly, from eqn (12), the terminal velocity of a subcritical shrinking loop with $r < a_1$ is positive, given by $a_1/a_3\tau$; however, this inference is not physically meaningful since, in the case of a reverse twist loop, it is not permissible to set $r = 0$, or indeed even $r < G/H$, which is the thread radius at which the defect loop would have shrunk to a point.

The time dependence of loop size is predicted to follow eqn (14) of Appendix A. For supercritical loops, as seen in Fig. 11, the observed time variation of diameter $D(t)$ fits this equation remarkably well. The fitted curve, which is based on the values of c and a_i appropriate to the experimental R_c value, corresponds to $\tau = 1.268 \text{ s}$ or $\gamma_1/k \approx 44 \text{ ms } \mu\text{m}^{-2}$. This γ_1/k is of the order expected from our previous measurements on 12OCN.¹² The same τ and a_i as determined for supercritical loops are used to obtain the fitted curve for subcritical loops in Fig. 11. Considering that eqn (12) becomes increasingly approximate as the annihilation of the loop is approached, the agreement between the fitted and observed data for shrinking loops is quite striking.

In the context of critical loop radius, it is relevant to mention an earlier interesting study⁶ on a rodlike, dielectrically and diamagnetically positive nematic. The sample here was in the form of a laterally concave globule confined between glass plates; the director was normal at all the limiting interfaces so that there existed a circular $-1/2$ disclination loop of radius R separating the inner pseudo isotropic and outer birefringent regions. With a rotating magnetic field B in the layer plane disfavoring the

homeotropic alignment, R could be reduced to some R_1 . On field removal, the loop either collapsed to a point defect at the centre or enlarged to the initial radius R depending, respectively, on whether R_1 was smaller or larger than a critical radius R_c . It is important to recognize that the loop here is a hybrid of the wedge and twist types and no manipulation with external fields can eliminate it to result in a defect free state. In other words, it is topologically equivalent to a monopole such as associated with a closed wedge disclination. This experiment⁶ is obviously different from the present one on pure twist loops with no net topological charge.

It is interesting to consider the stability of twist loops of higher strength. Evidently, $s = 1$ loops separating two opposite π -twisted, degenerate energy regions are unstable and collapse spontaneously to reduce the overall energy, just as an annular wall bridging degenerate oppositely tilted states. However, $s = 1$ loops between inner planar and enveloping 2π -twisted regions may be expected to possess a stationary energy state at a critical radius. As previously described (Fig. 6), 2π -twisted regions are generated during relaxation from a high energy disclination state. Surprisingly, we find spontaneous nucleation and growth of planar domains within these full-turn regions, implying the absence of an observable critical size. The time series of evolving birefringent states in Fig. 12, observed in the relaxing fluid at 120 °C after removal of a high field (100 V, 10 kHz), demonstrates this feature. In Fig. 12a, planar state is forming at sites A–C, within what eventually would be a 2π -twisted region. Planar domains at A–C are seen in Fig. 12b–d to grow monotonically. From a theoretical view point, broadly speaking, R_c is expected to be unaffected by a change in s from $1/2$ to 1, since this causes both the twist energy per unit area (proportional to the

square of the total twist angle) and the disclination energy per unit length (proportional to s^2) to increase to the same extent. What appears to be happening is that the system prefers two half strength loops at $z = (d/4, 3d/4)$ to a single unit strength loop at $z = d/2$ for energy reasons. This would reduce the critical radius to about half that for the π -twisted case. It is possible that the observed planar domains formed either at defect sites or *via* fluctuations are the ones with their initial size larger than the critical size. Further studies using thicker samples are necessary to definitively ascertain the existence of a critical size for the loops around planar domains in 2π -twisted regions.

Finally, it is necessary to note that, in principle, neither the generation of twist *via* pincement nor the theoretical prediction of critical size for L(P) can be exclusive to any particular class of mesogens. The elastic and viscous properties in individual cases will of course govern the nature of metastability, and render the observation and dynamical study of loops experimentally easier in some cases. For example, for bent-core nematogens, k_{33} is found much smaller relative to k_{11} ; it is also likely³³ that k_{22} is the lowest. Assuming twist and bend as dominant in the twist loops, the effective k would be small; since γ_1 is very large (ten times the value in usual calamitics), the relaxation time proportional to γ_1/k may be expected to be much larger than for rodlike mesogens. To demonstrate the validity of these remarks, we have included under ESI the experimental findings relating to the generation, stability and dynamics of loops L(P) in the rodlike nematic butyl 4-(4-ethoxyphenoxy carbonyl) phenyl carbonate (BEPC). The properties of these loops are very similar to those in 6OCN. For BEPC, R_c and γ_1/k are found to be about 15 μm and 4.6 ms μm^{-2} , respectively; the latter is an order lower than the corresponding value for 6OCN. Interestingly, the core radius (5.27 nm) for BEPC is approximately half that for 6OCN.

4 Conclusions

In this experimental study, firstly, we have described a novel method to generate π -twisted domains. It relies on the transformation of Brochard-Leger walls into a pair of disclination lines at the substrates, where the anchoring is planar, and the subsequent lateral separation of these lines. It is established that, on field removal, the region of separation, instead of returning to the base state, adopts the π -twisted state. Through this process, configurations of planar domains within π -twisted regions and *vice versa* are both realizable by a suitable choice of the field in the disclination state. It is important to note that, with thin samples, the twisted region exhibits a slight birefringence between crossed polarizers when the planar region is extinct. This is not an indication of any biaxiality of the type reported previously,³² but a consequence of the waveguide limitation. The director fields in the two regions are readily revealed through electroconvection patterns. Secondly, we have shown that, from the view point of stability and dynamics, twist loops encircling planar domains L(P) differ from those encircling π -twisted domains L(T). Loops L(T) shrink monotonically in accordance with the power law $R \propto (t_0 - t)^z$ and disappear at time t_0 ; significantly, the exponent is itself a function of the radius R , as previously predicted.⁹ Loops L(P), by

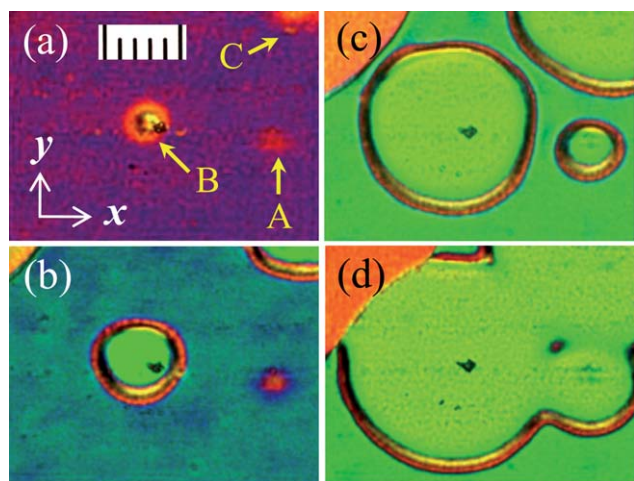


Fig. 12 (a–d) Time series of birefringent states observed between diagonally crossed polarizers in the relaxing fluid at 120 °C after removal of the applied high field (100 V, 10 kHz). (a) Metastable 2π -twist state evolving in the visual field; A–C are disturbed alignment regions wherein planar domains are nucleating. (b) Planar domains A–C growing monotonically with no indication of a critical size. (c) States with steady birefringence colours; the orange coloured region at the top left corner belongs to an enlarging π -twisted domain. (d) Light-green planar domains growing at the expense of twisted domains. 10 μm scale div.

contrast, exhibit an unstable equilibrium corresponding to a stationary energy state at a critical radius, as predicted very early.⁷ Such loops, generated and studied systematically for the first time both in bent-core and calamitic nematogens, are shown to possess a temperature varying R_c ; this points to the need for a theoretical description taking elastic anisotropy into account. There is also a need for determining the moduli k_{ii} to verify their involvement in the value of R_c . The growth and decay dynamics of loops L(P) across R_c are both shown to be completely explicable on the basis of the extended Sonnet-Virga model, which enables a determination of the parameter γ_1/k . It is further shown that the ‘electrical quenching’ process may also produce 2π -twisted domains and a variety of disclination lines between variously aligned regions.

A. Extension of the Sonnet-Virga model

The adaptation of the Sonnet-Virga model⁹ of half-strength loop disclinations L(T) encompassing π -twisted islands in planar layers to the case of inverse loops L(P) across which the director patterns are reversed requires the formal changes summarised here. We may schematically represent the director field for a loop L(P) as in Fig. 13(a), where the curves of equal alignment are obtained from Fig. 2 of ref. 9 by a reflection about the z -axis at the disclination. Beyond the radial distance R , the director turns uniformly through π between $-H$ and $+H$, with $|H| = d/2$. The loop of radius R in the sample midplane, termed the ‘thread’ for convenience, is coplanar with the singular loop of radius $R-G$.

The analysis is carried out with reference to the coordinate system depicted in Fig. 13(b), where the lines of equal alignment emanate from the defect line; $\theta = \arctan(z/\xi)$ is the angle between the ξ -axis and the line from the origin to the point (θ, λ) , λ being the parameter that specifies the equal alignment line on which the point lies. While the general separation between the thread and the defect line is given by $g = h/\sqrt{e}$, with the twisted region beyond R spanning between $-h$ and $+h$, the equilibrium separation, to which Fig. 13 applies, is given by $G = H/\sqrt{e}$. Assuming the director $\mathbf{n} = (\cos \varphi, \sin \varphi, 0)$, the following conditions on the angle φ are in order for the inverse loops:

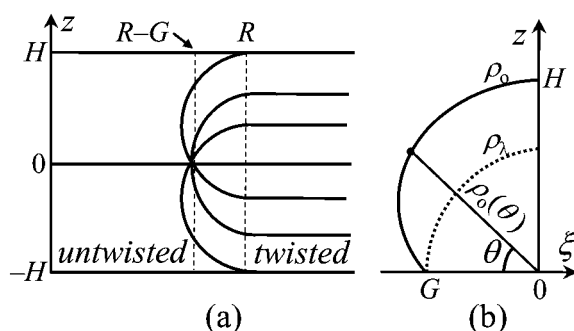


Fig. 13 (a) Curves of equal alignment for a circular disclination of strength $1/2$ located in the $z = 0$ plane and separating inner untwisted and outer π -twisted regions. R is the radial distance beyond which the twist is uniform. $R-G$ is the radius of the singular loop. (b) Coordinate system in terms of the curves of equal alignment. Only the upper half is depicted. All the equal alignment curves meet at the defect, with ρ_0 corresponding to $\varphi = 0$ and delineating the outer boundary of the disclination strain field.

$$\varphi = \begin{cases} 0 & \xi = 0, & z \geq h \\ \frac{\pi}{2} & z = 0, & -g < \xi \leq 0 \\ 0 & z = 0, & \xi < -g \end{cases}$$

While both ρ_λ and θ remain unchanged, eqn (13) of ref. 9 becomes $\xi = -\rho_\lambda(\theta) \cos \theta$. The total Frank-Oseen elastic free energy now reads

$$E = \frac{Ak}{h} \int_0^\infty \left(\frac{d\varphi}{d\lambda} \right)^2 e^\lambda d\lambda + \pi k \iint (\nabla\varphi)^2 (R - \xi) d\xi dz, \quad (8)$$

which is the same as eqn (45) of ref. 9 except for a change in the sign of the last term relating to the effect of curvature of the thread. This change in sign stems from the following reasoning. The integrand associated with the thread radius R , or the second term in eqn (8), neglects the effect of changing circumference or the curvature of the tubular region in which the strain energy resides. In the direct loop configuration,⁹ the thread is shorter than the defect line by $2\pi g$, and the rate of change of circumference over $2\pi R$ is positive; this accounts for a positive contribution by the last term in eqn (8), which caters to the curvature. Once the director patterns across the loop are inverted, the thread is longer than the singular line by $2\pi g$ and the rate of change of circumference relative to $2\pi R$ is negative; therefore, the contribution we are considering becomes negative. The first term giving the contribution E_A from the twisted region beyond R is, as in the case of loops L(T), given by $E_A = \pi^2 Ak/4h$, but here the area A takes the form $A = \pi(R_\infty^2 - R^2)$, where R_∞ may be thought of as the radius of some external lateral boundary of the twisted sample region. With these considerations, for L(P), eqn (52) of ref. 9 may be replaced, under equilibrium ($g = G$, $h = H = d/2$), by

$$E = \frac{\pi^3 k}{2d} (R_\infty^2 - R^2) + 2\pi R E_t - \pi k E_\sigma \quad (9)$$

where E_t and E_σ are, as in eqn (39), (46) and (51) of ref. 9, given by

$$E_t = \frac{\pi k}{8} \left(\frac{\pi^2 + 4}{4} F_G - 2 \right); \quad E_\sigma = \frac{d}{2} \left(\frac{\pi^3 + 4\pi}{16\sqrt{e}} F_G - 2.13 \right) \quad (10)$$

where $F_G = \ln(\pi G/c) = \ln[\pi d/(2c\sqrt{e})]$. It is to be noted that E in eqn (9) is the excess energy relative to the energy of the planar state. The excess energy relative to the π -twisted base state, such as considered by Friedel and de Gennes⁷ in eqn (6), is obtained by simply dropping R_∞^2 in eqn (9).

Following a similar reasoning in solving for the total viscous dissipation W in eqn (67) of ref. 9, we replace eqn (68) therein by

$$W = \frac{\pi^4}{8} \gamma_1 \dot{R}^2 \left[(F_G - 1.13)R - (F_G - 1.23) \frac{H}{\sqrt{e}} \right] \quad (11)$$

By eqn (9) and (11) above, and the dissipation principle that takes the form $W = -(dE/dt)$, we arrive at

$$\dot{r} = \frac{r - a_1}{\tau(a_2 r - a_3)}, \quad (12)$$

where a_1 , a_2 , a_3 , and τ are just the same as given by eqn (70)–(73) of ref. 9:

$$a_1 = \frac{\pi^2 + 4}{8\pi} F_G - \frac{1}{\pi}, \quad a_2 = F_G - 1.13, \\ a_3 = \frac{1}{\sqrt{e}} (F_G - 1.23); \text{ and } \tau = \frac{\pi \gamma_1 d^2}{16k}. \quad (13)$$

From eqn (13), we obtain the time dependence of the loop radius

$$\frac{t_r - t}{\tau} = a_2(r_r - r) + (a_1 a_2 - a_3) \ln \left(\frac{r_r - a_1}{r - a_1} \right), \quad (14)$$

where t_r is an arbitrary reference time at which the scaled radius is r_r .

Acknowledgements

It is a pleasure to acknowledge A. M. Sonnet (*Department of Mathematics and Statistics, University of Strathclyde, Livingstone Tower, 26 Richmond Street, Glasgow G1 1XH, Scotland, UK*) and E. G. Virga (*Dipartimento di Matematica, Università di Pavia, via Ferrata 1, I-27100 Pavia, Italy*) as our coauthors for Appendix A given above. We thank K. A. Suresh for the experimental facilities and G. S. Ranganath for useful discussions. We are indebted to R. B. Meyer, M. Kleman and O. D. Lavrentovich for valuable information on twist loops.

References

- 1 M. Kleman and J. Friedel, *Rev. Mod. Phys.*, 2008, **80**, 61.
- 2 M. Kleman, *Forms of matter and forms of Radiation*, arXiv:0905.4643v1 [gr-qc] 28 May 2009, <http://arxiv.org/find/all/1/au:+kleman/0/1/0/all/0/1>.
- 3 P. G. de Gennes and J. Prost, *The Physics of Liquid Crystals*, Oxford University Press, Oxford, 2nd edn, 1993.
- 4 E. M. Terentjev, *Phys. Rev. E: Stat., Nonlinear, Soft Matter Phys.*, 1995, **51**, 1330.
- 5 M. Kleman and O. D. Lavrentovich, *Soft Matter Physics*, Springer-Verlag, New York, 2003.
- 6 S. Thiberge, C. Chevillard, J. M. Gilli and A. Buka, *Liq. Cryst.*, 1999, **26**, 1225.
- 7 J. Friedel and P. G. de Gennes, *C.R. Acad. Sc. Paris B*, 1969, **268**, 257.
- 8 I. Chuang, N. Turok and B. Yurke, *Phys. Rev. Lett.*, 1991, **66**, 2472.
- 9 A. M. Sonnet and E. G. Virga, *Phys. Rev. E: Stat., Nonlinear, Soft Matter Phys.*, 1997, **56**, 6834.
- 10 B. Diao, K. Matsuoka and G. C. Berry, In *Keynote lectures in selected topics of polymer science*, Ed. E. Riande, National Council of Scientific Research of Spain, Madrid, 1995; Z. Tan, B. Diao and G. C. Berry, *Macromolecules*, 1999, **32**, 7172.
- 11 L. Kovalenko, M. W. Schroder, R. A. Reddy, S. Diele, G. Pelzl and W. Weissflog, *Liq. Cryst.*, 2005, **32**, 857.
- 12 P. Tadapatri, U. S. Hiremath, C. V. Yelamaggad and K. S. Krishnamurthy, *J. Phys. Chem. B*, 2010, **114**, 1745.
- 13 P. Tadapatri, K. S. Krishnamurthy and W. Weissflog, *Phys. Rev. E: Stat., Nonlinear, Soft Matter Phys.*, 2010, **82**, 031706.
- 14 E. Bodenschatz, W. Zimmermann and L. Kramer, *J. Phys. (Paris)*, 1988, **49**, 1875.
- 15 F. Brochard, *J. de Phys.*, 1972, **33**, 607.
- 16 L. Leger, *Solid State Commun.*, 1972, **11**, 1499.
- 17 K. S. Krishnamurthy and M. S. Bhate, *Mol. Cryst. Liq. Cryst.*, 1985, **128**, 29.
- 18 A. Stieb, G. Baur and G. Meier, *J. de Phys., Colloq. C1*, 1975, **36**, 185.
- 19 W. Helfrich, *J. Chem. Phys.*, 1969, **51**, 4092.
- 20 J. Nehring, *Phys. Rev. A: At., Mol., Opt. Phys.*, 1973, **7**, 1737.
- 21 A. de Lózar, W. Schöpf, I. Rehberg, D. Svesek and L. Kramer, *Phys. Rev. E: Stat., Nonlinear, Soft Matter Phys.*, 2005, **72**, 051713.
- 22 Ph. M. Lagarde, H. D. Lambez and I. Dozov, *Phys. Rev. E: Stat., Nonlinear, Soft Matter Phys.*, 2003, **67**, 051710.
- 23 S. Chandrasekhar and G. S. Ranganath, *Adv. Phys.*, 1986, **35**, 507.
- 24 C. Blanc, D. Svesek, S. Zumer and M. Nobili, *Phys. Rev. Lett.*, 2005, **95**, 097802.
- 25 K. S. Krishnamurthy and R. Balakrishna, *Pramana*, 2003, **61**, 270.
- 26 I. Chuang, B. Yurke, N. Pargellis and N. Turok, *Phys. Rev. E: Stat., Nonlinear, Soft Matter Phys.*, 1993, **47**, 3343.
- 27 M. A. Shahzamanian and E. Kadivar, *Mol. Cryst. Liq. Cryst.*, 2006, **457**, 83.
- 28 W. Wang, T. Shiwaiku and T. Hashimoto, *J. Chem. Phys.*, 1998, **108**, 1618.
- 29 N. Osterman, J. Kotar, E. M. Terentjev and P. Cicutta, *Phys. Rev. E: Stat., Nonlinear, Soft Matter Phys.*, 2010, **81**, 061701.
- 30 This is an approximate version of the self inductance of a circular conductor given, in cgs emu, by $L = 4\pi R[\ln(8R/c) - 2]$. See, e.g., W. Greiner, *Electrodynamics*, Springer, New York, 1993.
- 31 M. J. Stephen and J. P. Straley, *Rev. Mod. Phys.*, 1974, **46**, 617. Here, $L = 4\pi R \ln(8R/c)$ is assumed and the critical radius is written as $R_c = (\ln 2/qc)/4q$.
- 32 R. Stannarius, A. Eremin, M.-G. Tamba, G. Pelzl and W. Weissflog, *Phys. Rev. E: Stat., Nonlinear, Soft Matter Phys.*, 2007, **76**, 061704.
- 33 M. Majumdar, P. Salamon, A. Jakli, J. T. Gleeson and S. Sprunt, *Phys. Rev. E: Stat., Nonlinear, Soft Matter Phys.*, 2011, **83**, 031701.